Sensors and Actuators A 275 (2018) 99–108

Contents lists available at ScienceDirect

Sensors and Actuators A: Physical

journal homepage: www.elsevier.com/locate/sna

Electrostatic compensation of structural imperfections in dynamically amplified dual-mass gyroscope

Alexandra Efimovskaya*, Danmeng Wang, Yu-Wei Lin, Andrei M. Shkel

MicroSystems Laboratory, Department of Mechanical and Aerospace Engineering, University of California, Irvine, CA, USA

ARTICLE INFO

Article history:
Received 23 October 2017
Received in revised form 3 February 2018
Accepted 2 March 2018
Available online 28 March 2018

Keywords:
MEMS gyroscope
Dual-mass system
Precision electrostatic tuning
Fabrication imperfections
Anisoelasticity
Frequency split

ABSTRACT

This paper presents a study on dynamics of a dual-mass MEMS vibratory gyroscope in presence of fabrication imperfections and reports a method for precision electrostatic frequency tuning of the operational modes. A number of multi-mass MEMS gyroscopes have emerged in recent years pursuing different goals, such as dynamically balanced structure, increased bandwidth, and dynamic amplification. Along with many perceived advantages of multi-mass devices, several challenges associated with mode-matching in a system with increased number of degrees-of-freedom (DOF) have to be considered. This work shows that it is possible to apply the DC tuning techniques, similar to tuning a conventional single-mass gyroscope, to achieve the precision tuning in a dual-mass sensor, without losing advantages of increased DOF of the system. The presented frequency trimming technique is based on assessing the modes mismatch and cross-coupling between modes by means of fitting the experimental frequency response curves to the analytical solutions of the dual-mass system in presence of imperfections. The tuning algorithm involves two steps. First, the stiffness mismatch along the two axes and the anisoelasticity angles α and β are identified, then the tuning DC voltages for modification of diagonal, off-diagonal, and coupling terms in the stiffness matrix are chosen. The method of electrostatic tuning was validated through the experimental characterization of a dual-mass dynamically amplified gyroscope, where the coupling between the two operational modes was minimized and frequency split was reduced from 26 Hz down to 50 mHz, resulting in 17.5× increase in the gyroscope scale factor and significantly improved noise characteristics. The presented electrostatic compensation method is suitable for both off-line and on-line calibration.

1. Introduction

Conceptually, a single-axis gyroscope requires a single proof-mass for measuring the Coriolis acceleration induced angular rate signal. In recent years, however, a variety of multi-mass solutions emerged offering advantages, such as dynamic balance, Fig. 1(a), increased bandwidth, Fig. 1(b), and dynamic amplification, Fig. 1(c).

Dynamically balanced systems, Fig. 1(a), such as, for example, the Dual Foucault Pendulum (DFP) gyroscope [1], utilize two, four or more dynamically equivalent, mechanically coupled proof-masses, oscillating in anti-phase motion, for improved vibration immunity and anchor loss mitigation, resulting in ultra-high quality factor. The concept of dynamic balance for anchor loss mitigation and a common-mode rejection of shock and vibration is employed in the design of the Tuning Fork (TF) Gyroscope [2], where two dynamically equivalent mechanically coupled proof masses are utilized. A similar principal is employed in the design of a Quadruple Mass Gyroscope (QMG) [3], where the structural element is formed by four mechanically coupled proof-masses, enabling a dynamic balance of forces and moments in the anchor in both drive and sense modes.

Acar et al. demonstrated an increased bandwidth inherently robust dual-mass gyroscope [4]. The mechanical element was comprised of a two degree-of-freedom (DOF) sense-mode oscillator, formed by two interconnected masses, Fig. 1(b). The device was operated in the flat region of the sense-mode response curve, where the amplitude and phase of the response are insensitive to environmental fluctuations.

Another example of a multi-mass solution is a dual-mass dynamically amplified system, Fig. 1(c), where an increased number of degree-of-freedom (DOF) results in dynamic amplification of motion and improved sensitivity of the device [5,6].

Along with many advantages of the dual-mass systems, the structural symmetry is a challenge. The symmetric mechanical element is necessary for the mode-matched devices, and a method of compensation for fabrication imperfections is required.

* Corresponding author.
E-mail address: aefimovs@uci.edu (A. Efimovskaya).

https://doi.org/10.1016/j.sna.2018.03.001
0924-4247/

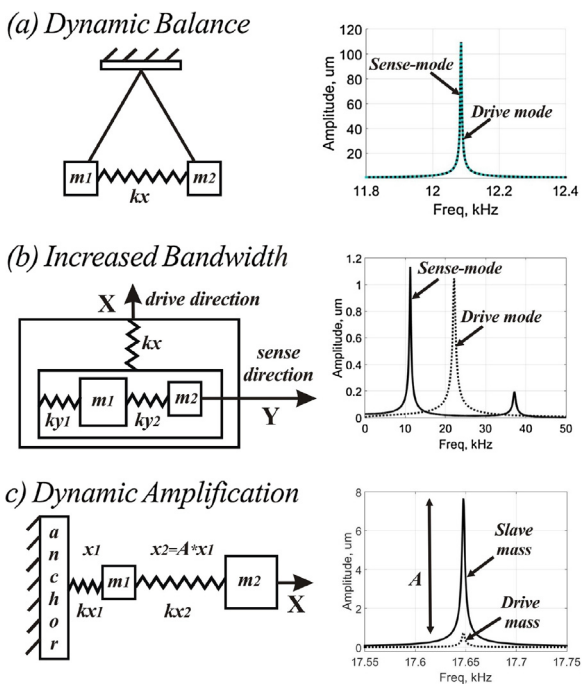

Fig. 1. Examples of multi-mass gyroscopes: (a) dynamically balanced two-mass system, (b) dual-mass system with 2-DOF sense-mode oscillator and (c) dynamically amplified system.

Most methods of matching the operational modes of the gyroscope can be divided in two general categories: passive techniques, such as post-processing mechanical trimming methods [9–13], and active techniques, such as electrothermal [14], feedback control, [15–17], and electrostatic tuning [18–33].

Mechanical trimming methods are based on a permanent modification of the structure by means of selective adding/removing material to/from the vibrational element. Such trimming can employ, for example, laser ablation [9,10], focused ion beam [11], and selective deposition [12,13]. The main advantage of this technique is a permanent change of the sensor structure, enabling minimization of voltages necessary for subsequent electrostatic tuning. The passive tuning method, however, is mainly limited to off-line calibration in a laboratory environment.

In contrast to the mechanical trimming, active tuning techniques do not introduce a permanent modification of the structure, do not require expensive precision trimming equipment, and can be implemented in real-time after the sensor is packaged, including during an on-line in-field calibration. A method of active thermal tuning for microresonators using resistive heaters to generate localized thermal stresses in the structure is described in [14]. A number of active tuning approaches using feedback control for quadrature signal compensation [15], and precision mode matching [16,17], were reported in literature.

Electrostatic tuning, which employs electrostatic force gradients to selectively modify the effective stiffness of a certain operational mode, is a common active-tuning technique for the gyroscope mode-matching. The method has been extensively studied by different research groups. An active electrostatic "trimming" utilizing non-linearity of capacitive parallel-plate actuators was applied for frequency tuning and reduction of modes coupling in rate integrating gyroscopes [18]. An approach for electrostatic tuning of the wineglass modes in MEMS ring gyroscopes was described in [19,20]. In these publications, the 16 tuning electrodes surrounding the ring structure were used to independently modify the diagonal and off-diagonal terms of the structural stiffness matrix and to achieve a reduction of the frequency split between the modes. Electrostatic tuning has been successfully used for many other different types of planar [1,23–28], and three-dimensional structures [29–33].

The focus of this paper is on precision electrostatic tuning of the operational modes in a gyroscope with a dual-mass structural element. Most of the electrostatic tuning methods, previously described in the literature, considered a 2-degrees-of-freedom system with a 2×2 stiffness matrix [18–20]. However, increasing the number of proof-masses in a gyroscope results in a more complex form of the system's stiffness matrix. Hence, new algorithms have to be developed for precision electrostatic tuning. In this paper, we study the dynamics of an imperfect dual-mass system, using as an example a dynamically amplified MEMS gyroscope. A method of electrostatic frequency tuning in such multi-degree of freedom system is described and experimental verification of the proposed approach is presented.

In the following sections, we will first introduce the dynamic amplification concept, Section 2. We will then present the design of a dynamically amplified gyroscope, which is used for illustration of the frequency tuning algorithm, Section 3. In the same Section 3, we will also derive dynamic equations of a dual-mass system and report results of experimental characterization of the fabricated prototypes, demonstrating the amplitude amplification phenomenon. In Section 4, we will describe an algorithm for the precision electrostatic tuning of a dual-mass dynamically amplified gyroscope and provide experimental verification of the proposed approach. Introduction of the tuning algorithm will be followed by comparison of the sensor performance, before and after electrostatic tuning, in Section 5. Section 6 concludes the paper with a discussion on applicability of the presented electrostatic compensation technique.

2. Dynamic amplification concept

Dynamic amplification of motion has been previously employed in design of MEMS structures. Mechanical lever has been utilized in resonant and quasi-static accelerometers to enhance sensitivity through force [21], and displacement amplification [22]. In principal, a lever can be used for motion amplification in gyroscopes, however, due to the requirement of symmetry and degeneracy of operational modes, it is difficult to implement a displacement-amplifying lever in design of an angle-measuring device.

Alternatively, a coupled dual-mass system can be used for motion amplification [5,6]. A dual mass-spring model of a simple dynamically amplified system is shown in Fig. 1(c). The system is comprised of two mechanically coupled proof-masses: drive mass m_1 and slave mass m_2. Here, k_{x1} is the spring constant of coupling between the mass m_1 and the anchor, k_{x2} is the spring constant of coupling between the two proof-masses. The dynamic equations of motion for this system can be expressed as:

$$\begin{aligned} &m_1\ddot{x}_1 + c_1\dot{x}_1 + (k_{x1} + k_{x2})x_1 - k_{x2}x_2 = F_{x1}; \\ &m_2\ddot{x}_2 + c_2\dot{x}_2 + k_{x2}x_2 - k_{x2}x_1 = 0, \end{aligned} \tag{1}$$

where c_1 and c_2 are the damping coefficients of the drive and the slave masses, respectively. F_{x1} is the external force applied to the drive mass.

The system of Eq. (1) can be solved with respect to the ratio between the amplitudes of the drive and slave masses [5]:

$$A = \frac{X_2}{X_1} = \frac{k_{x2}}{k_{x2} + c_2(i\omega) - m_2\omega^2}, \tag{2}$$

where ω is the frequency of an external force applied to the drive mass. The frequency of the driving force is the first resonant frequency of the coupled dual-mass system (Fig. 2), where

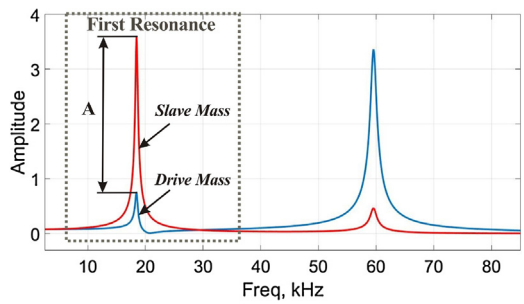

Fig. 2. Dynamic amplification at the first resonant frequency of the coupled dual-mass system.

the dynamic amplification condition ($A > 1$) is satisfied and high deflections of the slave mass can be achieved:

$$\omega = \frac{1}{2}\left[\frac{k_{x1}+k_{x2}}{m_1}+\frac{k_{x2}}{m_2}\right] - \frac{1}{2}\sqrt{\frac{(k_{x1}+k_{x2})^2}{m_1^2}+\frac{k_{x2}^2}{m_2^2}-\frac{2k_{x2}(k_{x1}-k_{x2})}{m_1 m_2}}. \quad (3)$$

From Eqs. (2) and (3), it can be concluded that in order to maximize the dynamic amplification factor A, the spring constant k_{x2}, the damping coefficient c_2, and mass m_1 have to be reduced, while the spring constant k_{x1} and mass m_2 have to be increased.

3. Dynamically amplified gyroscope

3.1. Design and fabrication

The dynamic amplification concept can be applied in design of a MEMS gyroscope with a dual-mass architecture (Fig. 3), where the increase in structural degrees of freedom is used to improve sensitivity, linearity, and to reduce drift [5,6]. In a dynamically amplified gyroscope, the first, the"drive mass", is actively driven to oscillate at a small amplitude of motion, in a linear operational regime. Meanwhile, the mechanically coupled "slave mass" is used for sensing the Coriolis signal. The amplitude of motion of the "slave mass" is dynamically amplified resulting in increased scale factor of the gyroscope.

The gyroscope prototypes have a footprint of 7.4 mm × 7.4 mm. The design parameters are summarized in Table 1. In order to investigate the dependence of the sensor dynamic amplification factor on structural imperfections in the system, two designs of the gyroscope were studied, providing the dynamic amplification of 5× (Design I) and 10× (Design II). The sensor is comprised of

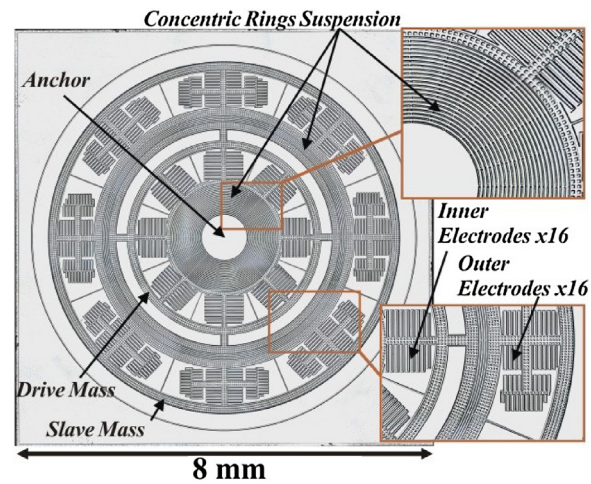

Fig. 3. Micro-photograph of a fabricated prototype of the dynamically amplified dual-mass gyroscope [8].

an inner, "drive mass", and an outer, "slave mass", mechanically connected by means of the concentric rings suspension. The outer suspension is formed by 18 μm thick concentric rings between the two masses. The inner suspension is also formed by 18 μm thick concentric rings, connecting the inner mass to the center anchor.

Each proof-mass is surrounded by 16 electrodes with parallel plates for drive and pick-off. The capacitive parallel-plate actuators are also used for frequency tuning through the electrostatic spring-softening effect [7]. To provide close-to-a-linear driving regime, devices are electrostatically driven to oscillate with small amplitudes of a driving mass: 300 nm and 150 nm, correspondingly, for Design I and Design II. Dynamic amplification results in high amplitude of motion of the outer mass: 1.5 μm for both designs.

The nominal capacitive gap between the parallel plates is 5 μm. The minimum gap of the sensor is limited by the aspect ratio of the DRIE etching process, which is currently 20:1. A reduced nominal gap in thinner than 100 μm device layer could be used for improved transduction factor for the drive, sense and tuning electrodes. However, reduction of the structural layer thickness leads to lowered out-of-plane modes and, as a result, degraded environmental performance.

The two proof-masses are driven to oscillate in in-phase motion, Fig. 4. Devices were designed to operate at the resonant frequency of 17.5 kHz.

The axisymmetric dynamically amplified gyroscope can operate in a rate or an angle measuring mode, Fig. 5. In the rate measuring mode of operation, the drive and sense modes consist of the

Table 1
Design parameters of the dynamically amplified gyroscope.

	Design I	Design II
Dynamic amplification	5×	10×
Footprint, mm^2	7.4 × 7.4	7.4 × 7.4
Drive mass, kg	1.23e−6	1.23e−6
Slave mass, kg	2.07e−6	2.07e−6
Operational frequency (1st resonance of a dual-mass system in Fig. 2), kHz	17.2	19.3
2nd resonance of a dual-mass system in Fig. 2, kHz	52.4	65.8
Number of rings in inner suspension	22	7
Number of rings in outer suspension	4	4
Width of rings, μm	18	18
Stiffness k_1, kN/m	84.9	166.8
Stiffness k_2, kN/m	43.4	43.4
Capacitive gap, μm	5	5
Total inner capacitance, pF	7.21	7.21
Total outer capacitance, pF	16.5	16.5
Q TED limited	90k	105k
Q air-damping limited (at 0.12 μTorr)	3.3 M	4 M

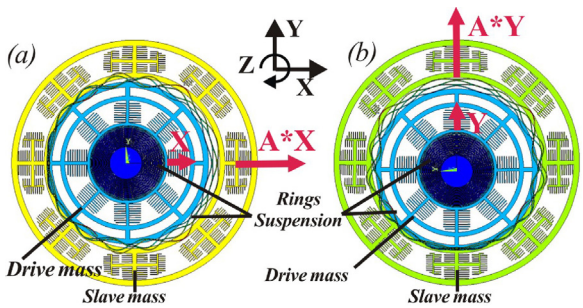

Fig. 4. FEA model, showing a characteristic motion of "drive mass" and in-phase amplified motion of "slave" mass in (a) drive-mode direction and (b) sense-mode direction.

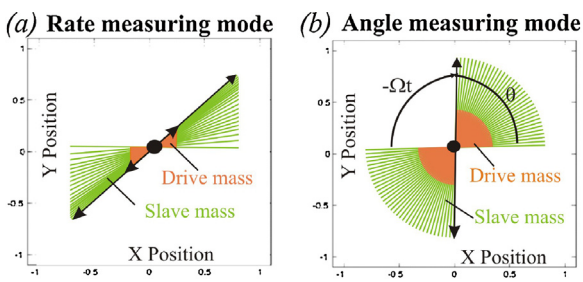

Fig. 5. (a) In rate measuring mode, sense deflection (*Y*-axis) is proportional to the input angular rate and (b) in angle measuring mode, angle of precession follows the negative angle of rotation (or, equivalently, preserves its orientation of vibration in the absolute-inertial coordinate frame).

translational motion of the driving mass, and dynamically amplified in-phase translational motion of the "slave mass" along the *X* and *Y* axes, correspondingly, Fig. 5(a). The mechanical element is driven to oscillate in drive mode along the *X* direction. The sense mode oscillations (along the *Y* direction) are induced by the Coriolis force due to inertial rotation. The amplitude of the slave mass deflection along the *Y* axis is proportional to the input angular rate:

$$A^{y}_{slave} = 2\ \mathrm{k}\Omega A^{x}_{slave} \frac{Q_y}{\omega_y \sqrt{1 + (2Q_y \Delta\omega/\omega_y)^2}}, \tag{4}$$

where A^{x}_{slave} is the dynamically amplified amplitude of oscillations of the "slave" mass along the *X* direction, *k* is the sensor's angular gain factor, Ω is the applied angular rate, ω_y and Q_y are the sense mode natural frequency and quality factor, respectively, $\Delta\omega$ is the frequency mismatch between the modes.

For a high quality factor and a small frequency split between the operational modes, considering an angle gain factor $k = 1$, Eq. (4) can be reduced to a standard equation for sense-mode displacement of a mode-matched gyroscope [36,38];

$$y = 2x\Omega \frac{Q_y}{\omega}. \tag{5}$$

Here the displacement *x* is defined by the amplitude of dynamically amplified oscillations of the "slave" mass along the *X* direction.

In the rate integrating mode of operation, the in-phase translational motion of the two proof-masses is free and unconstrained, while the motion of the slave mass is dynamically amplified. Generally, the trajectory of free oscillations is an elliptical orbit (or a straight line, in an ideal case). When an angular rotation is applied, Fig. 5(b), the line of oscillation of the two proof-masses starts processing in presence of the Coriolis force, legging behind the rotation with the precession coefficient *k*, defined by the sensor geometry [36]:

$$\theta = -k \int \Omega(\tau) d\tau, \tag{6}$$

where *k* is called the sensor angular gain factor and Ω is the applied angular rotation. For the rate integrating mode of operation, the angular rate drift of the gyroscope can be expressed as [39]:

$$\dot{\theta} \le \frac{1}{2} \left| \Delta \left(\frac{1}{\tau} \right) \right| + \frac{q}{A_{slave}} \left| \Delta\omega \right|, \tag{7}$$

where $\left|\Delta\left(\frac{1}{\tau}\right)\right|$ is the difference in damping coefficients along the two principal directions of vibration, $\left|\Delta\omega\right|$ is the frequency split between the two modes of vibration, A_{slave} is the amplitude of oscillation along the major diagonal of the elliptical orbit, q is the amplitude of oscillation along the minor diagonal of the elliptical orbit.

From Eqs. (4) and (7), it can be concluded that dynamic amplification is beneficial for both the angular rate and the angle measuring modes of operation since it allows for improved scale factor and reduced drift of the gyroscope.

In a dual-mass architecture the drive mass is actuated at a small amplitude of motion, allowing to preserve the linearity of the capacitive parallel-plate drive. Meanwhile, dynamic amplification in a coupled system allows for the slave mass to respond to the drive mass motion with an amplified amplitude, resulting in enhanced sensitivity.

In [37], the performance of the dual-mass gyroscope with amplitude amplification architecture was compared to a single-mass sensor of the similar footprint with a similar nominal capacitance, and equal frequency split between the operational modes. Both gyroscopes were driven to the same amplitude of vibration, and the experimental characterization showed 3× larger scale factor, 2.8× lower bias instability, and 2.5× lower Angle Random Walk (ARW) of the dual-mass gyroscope as compared to a single-mass device.

Prototypes of the dynamically amplified gyroscope, Fig. 3, were fabricated on a wafer-level using a single-mask SOI fabrication process with a 100 μm thick device layer and using a 1.5 μm thick thermal oxide layer as a hard mask for the Deep Reactive Ion Etching (DRIE) of silicon. The SPTS APS PM tool was utilized to define the silicon dioxide hard mask, while STS System DRIE was utilized for etching the silicon device layer. Once the fabrication process was complete, the wafers were diced using an ultra-clean stealth dicing method. The sensors were then released using a stiction-free vapor HF process (for 1 hr 15 min at 45 °C temperature) and packaged in ceramic Leadless Chip Carrier (LCC) packages.

3.2. Equations of motion

The dynamics of a dual-mass system is analyzed in the non-inertial coordinate frame associated with the gyroscope (the coordinate frame attached to the outer frame of the die). The equations of motion are derived using a dual mass-spring-damper model. In an "ideal" case (Fig. 6(a)), when damping, stiffness mismatch, and structural anisoelasticity are ignored, the governing

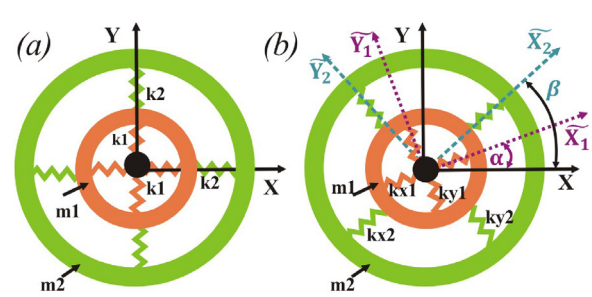

Fig. 6. (a) "Ideal" dual-mass system, when damping, stiffness mismatch, and structural anisoelasticity are not considered and (b) imperfections in suspension and mass cause the misalignment of the principal axes of elasticity.

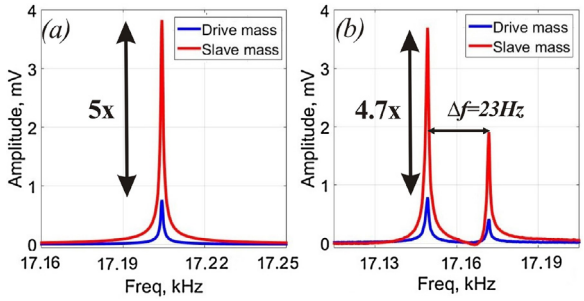

Fig. 7. Gyroscope Design I: (a) simulated freq. response with predicted amplification of 5× and (b) experimental response with coupling of drive and sense modes: Δf = 26 Hz; amplification 4.7×.

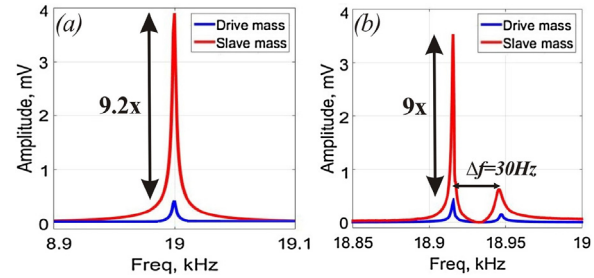

Fig. 8. Gyroscope Design II: (a) simulated freq. response with predicted amplification of 9.2× and (b) experimental response with coupling of drive and sense modes: Δf = 30 Hz; amplification 9×.

equations of motion of a gyroscope, measuring rotation about the Z-axis, are expressed in a matrix form as

$$[M]\ddot{q} + [C]\dot{q} + [K]q + [R_c]\dot{q} = [F], \tag{8}$$

where q is the vector of the generalized coordinates $q = [x_1 y_1 x_2 y_2]^T$. The generalized mass and damping matrices have the structure:

$$M = \begin{bmatrix} m_1 & 0 & 0 & 0 \\ 0 & m_1 & 0 & 0 \\ 0 & 0 & m_2 & 0 \\ 0 & 0 & 0 & m_2 \end{bmatrix}, \quad C = \begin{bmatrix} c_1 & 0 & 0 & 0 \\ 0 & c_1 & 0 & 0 \\ 0 & 0 & c_2 & 0 \\ 0 & 0 & 0 & c_2 \end{bmatrix}$$

The external force vector and the Coriolis force matrix have the structure:

$$F = \begin{bmatrix} F_{x1} \\ F_{y1} \\ 0 \\ 0 \end{bmatrix}, \quad R_c = \begin{bmatrix} 0 & -2m_1\Omega & 0 & 0 \\ 2m_1\Omega & 0 & 0 & 0 \\ 0 & 0 & 0 & -2m_2\Omega \\ 0 & 0 & 2m_2\Omega & 0 \end{bmatrix},$$

where Ω is the angular rate applied around the Z axis.

Finally, the generalized stiffness matrix has the structure:

$$K = \begin{bmatrix} k_1 + k_2 & 0 & -k_2 & 0 \\ 0 & k_1 + k_2 & 0 & -k_2 \\ -k_2 & 0 & k_2 & 0 \\ 0 & -k_2 & 0 & k_2 \end{bmatrix}, \tag{9}$$

where k_1 and k_2 are the stiffness coefficients for the inner and the outer mass suspension, correspondingly.

3.3. Experimental demonstration of dynamic amplification

Experimental frequency response of the sensor was obtained using electrostatic excitation with 10 V DC voltage and 60 mV AC voltage, applied to the driving electrodes of the inner mass. Design I devices were designed to operate at the resonant frequency of 17.5 kHz and to provide the dynamic amplification of 5×, Fig. 7(a). Characterization of the fabricated Design I prototype revealed the central frequency of 17.44 kHz with the amplification factor of 4.7× and the frequency split (Δf) of 26 Hz, Fig. 7(b). Design II devices were designed to operate at the resonant frequency of 19 kHz and to provide the dynamic amplification of 9.2×, Fig. 8(a). Characterization of the fabricated Design II prototype revealed the central frequency of 18.93 kHz with the amplification factor of 9× and the frequency split (Δf) of 30 Hz, Fig. 7(b).

For the drive and slave masses in Figs. 7(b) and 8(b), the first peak on the sense-mode frequency response curves corresponds to the frequency of the sense mode, the second peak corresponds to the frequency of the drive mode and is caused by the coupling of the drive motion to the sense mode. This coupling leads to the energy distribution between the modes and results in reduced amplitude amplification factor as compared to the analytically predicted, 4.7× vs 5×, Fig. 7, and 9× vs 9.2×, Fig. 8. It is important to notice that a stronger coupling between the drive and sense modes of the Design I prototype resulted in higher drop in the amplification factor, as compared to the Design II prototype.

4. Electrostatic correction of structural imperfections

Experimental frequency characterization of 12 prototypes from the same fabrication run revealed a frequency split between the modes (Δf) in the range from 25 Hz to 59 Hz, which arises from fabrication-induced asymmetries in the mechanical element.

Mode splitting is defined mainly by the etching uniformity of DRIE process and accuracy of the etching mask. The sensors features of the thermal oxide etching mask are defined with high precision, using Shipley 1827 photoresist lithography, followed by oxide etching and photoresist stripping. To improve the etching uniformity, the uniform gaps and uniform loading across the device and across a wafer are used. In addition, similar to the designs with a concentrated suspension architecture [40], concentric rings enable further reduction of frequency splits induced by Si etching non-uniformity.

Frequency splits are generally different across a wafer, across the different designs and across the different fabrication runs, ranging from 1.5 Hz to 150 Hz for UCI "in-house" fabricated dynamically amplified devices. In the following section, the method of electrostatic correction of structural imperfections will be introduced and utilized to tune the Design I gyroscope prototype, Fig. 7.

In case of a dual-mass gyroscope, the structural symmetry is defined by a 4 × 4 stiffness matrix, Eq. (5). Imperfections in suspension and mass cause the misalignment of the principal axes of elasticity [34,35] of both masses, resulting in non-zero off-diagonal terms of the stiffness matrix and increased coupling between the drive and sense modes, Figs. 7(b) and 8(b). Fabrication imperfections of both masses also result in non-equal diagonal terms of the stiffness matrix, leading to frequency splits between the modes. The resulting generalized stiffness matrix for the dual-mass system in presence of imperfections has the structure:

$$K = \begin{bmatrix} k_{11} & k_{12} & k_{13} & k_{14} \\ k_{12} & k_{22} & k_{23} & k_{24} \\ k_{13} & k_{23} & k_{33} & k_{34} \\ k_{14} & k_{24} & k_{34} & k_{44} \end{bmatrix}, \tag{10}$$

where the diagonal terms are:

$$k_{11} = \cos^2\alpha(k_{x1} + k_{x2}) + \sin^2\alpha(k_{y1} + k_{y2}),$$

$$k_{22} = \sin^2\alpha(k_{x1} + k_{x2}) + \cos^2\alpha(k_{y1} + k_{y2}),$$

$$k_{33} = \cos^2\beta * k_{x2} + \sin^2\beta * k_{y2},$$

$$k_{44} = \sin^2\beta * k_{x2} + \cos^2\beta * k_{y2};$$

the off-diagonal terms are:

$$k_{12} = 0.5 * \sin 2\alpha(k_{x1} + k_{x2} - k_{y1} - k_{y2}),$$

$$k_{34} = 0.5 * \sin 2\beta(k_{x2} - k_{y2});$$

and the coupling terms are:

$$k_{13} = -k_{x2}\cos\beta * \cos\alpha - k_{y2}\sin\beta * \sin\alpha;$$

$$k_{14} = -k_{x2}\sin\beta * \cos\alpha + k_{y2}\cos\beta * \sin\alpha;$$

$$k_{23} = -k_{x2}\cos\beta * \sin\alpha + k_{y2}\sin\beta * \cos\alpha;$$

$$k_{24} = -k_{x2}\sin\beta * \sin\alpha - k_{y2}\cos\beta * \cos\alpha.$$

Here α and β are the anisoelasticity angles for the inner and outer masses; k_{x1} and k_{x2} are the stiffness coefficients along the X axis for the inner and the outer mass suspension; k_{y1} and k_{y2} are the stiffness coefficients along the Y axis for the inner and the outer mass suspension, Fig. 6(b).

Our method for precision electrostatic frequency tuning of the operational modes is based on estimation of the anisoelasticity angles using the experimental frequency responses of the inner and outer proof-masses, followed by identification of the tuning voltages using an analytical solution of the dynamic equations in presence of imperfections:

$$[M]\ddot{q} + [C]\dot{q} + ([K] - [K_e])q + [R_c]\dot{q} = [F], \tag{11}$$

where $([K] - [K_e])$ is the electrostatically modified stiffness matrix.

To identify the anisoelasticity and modes mistuning parameters, the experimental frequency responses of the drive and slave masses were fitted to the analytical solutions of the dynamic Eq. (8) for the dual-mass system in presence of imperfections, Fig. 9. For one of the Design I gyroscope prototypes, with a 26 Hz frequency split (Δf) between the operational modes, the anisoelasticity angles $\alpha = 29^\circ$ and $\beta = 26^\circ$ were found. The aniso-elasticity angles α and $\beta > 22.5^\circ$ correspond the principal axes of elasticity closer to the diagonal electrodes. Generally, to reduce the voltages necessary for the subsequent tuning, the sensor's wire-bonding is changed, switching the directions of the drive and tuning electrodes. However, in order to estimate the tuning capabilities, for the sensor presented in this paper, the initial wire-bonding scheme was kept.

Next, using the Eq. (11), the terms of the matrix K_E for tuning the diagonal, off-diagonal, and coupling terms of the stiffness matrix were analytically identified and the necessary tuning voltages for the two masses were determined.

Electrostatic tuning matrix has the structure:

$$K_e = \begin{bmatrix} k_{e11} & k_{e12} & 0 & 0 \\ k_{e12} & k_{e22} & 0 & 0 \\ 0 & 0 & k_{e33} & k_{e34} \\ 0 & 0 & k_{e34} & k_{e44} \end{bmatrix}. \tag{12}$$

Configuration of the drive, the sense, and the tuning electrodes of a dynamically amplified dual-mass gyroscope is shown in Fig. 10.

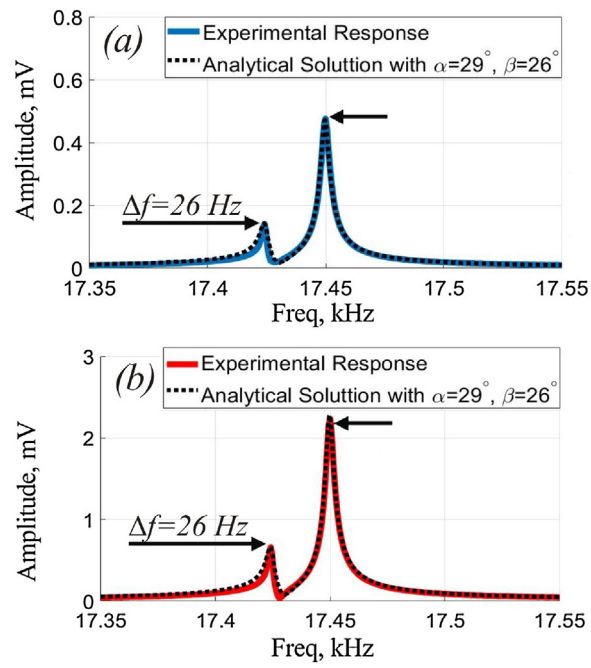

Fig. 9. Experimental frequency responses of (a) drive and (b) slave masses were fitted to the analytical solutions of the dynamic equations in presence of imperfections.

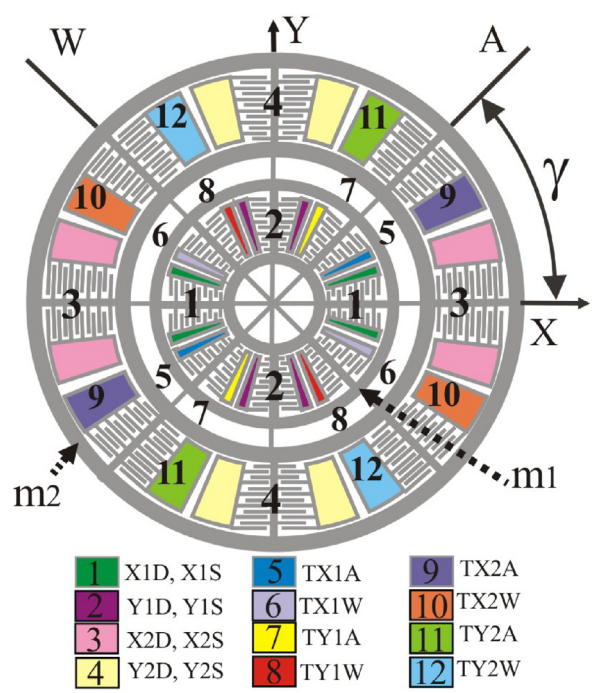

Fig. 10. Configuration of drive, sense and tuning electrodes of dynamically amplified dual-mass gyroscope.

Electrodes X1D, X1S and X2D, X2S are used for drive and/or signal pick-off along the X-axis for the mass m_1 and mass m_2, correspondingly. Electrodes Y1D, Y1S and Y2D, Y2S are used for drive and/or signal pick-off along the Y-axis for the mass m_1 and mass m_2, correspondingly. Electrodes TX1A, TX1W, TY1A, and TY1W are used for tuning the off-diagonal stiffness terms corresponding to the mass m_1. Electrodes TX2A, TX2W, TY2A, and TY2W are used for tuning the off-diagonal stiffness terms corresponding to the mass m_2.

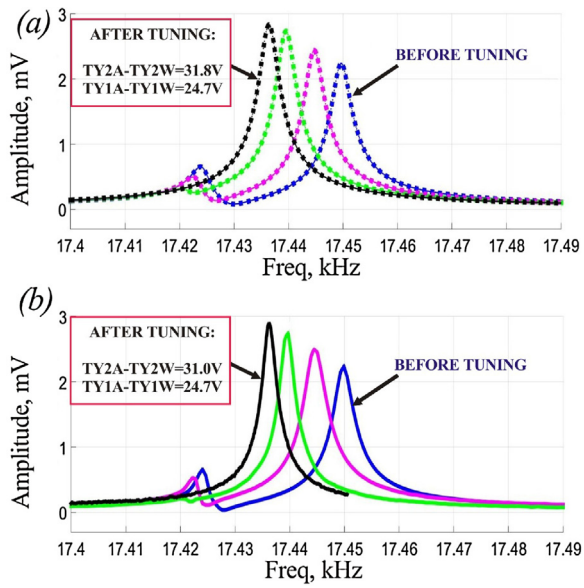

Fig. 11. Freq. response showing tuning of the off-diagonal terms of stiffness matrix and reduction of coupling between modes: (a) simulated and (b) experimental.

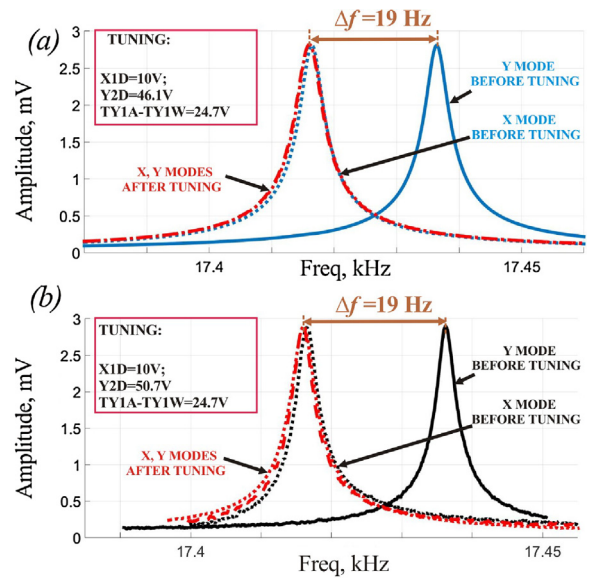

Fig. 12. Freq. response showing tuning of the diagonal terms of stiffness matrix and reduction of frequency split between modes: (a) simulated and (b) experimental.

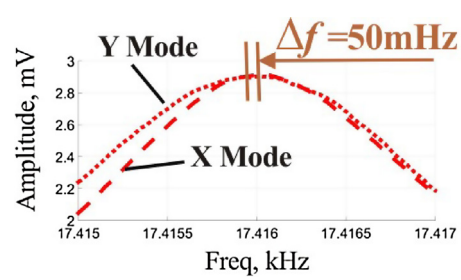

Fig. 13. Using simultaneous tuning of diagonal, off-diagonal, and coupling terms in stiffness matrix, the frequency split between the operational modes was reduced from 26 Hz down to 50 mHz (experimental result).

The terms of the electrostatic tuning matrix can be represented as:

$$k_{e11} = V_{x1}^2 + (\cos(\gamma))^2 T_{1a}^2 + (\cos(\gamma)^2 T_{1w}^2;$$

$$k_{e12} = \cos(\gamma)\sin(\gamma) T_{1a}^2 - \cos(\gamma)\sin(\gamma) T_{1w}^2;$$

$$k_{e22} = V_{y1}^2 + \sin((\gamma))^2 T_{1a}^2 - \sin((\gamma))^2 T_{1w}^2;$$

$$k_{e33} = V_{x2}^2 + \cos((\gamma))^2 T_{2a}^2 + \cos((\gamma))^2 T_{2w}^2;$$

$$k_{e34} = \cos(\gamma)\sin(\gamma) T_{2a}^2 - \cos(\gamma)\sin(\gamma) T_{2w}^2;$$

$$k_{e44} = V_{y2}^2 + \sin((\gamma))^2 T_{2a}^2 - \sin((\gamma))^2 T_{2w}^2,$$

where T_{1a} and T_{2a} are the tuning voltages applied to the mass m_1 and mass m_2 along the A-axis; T_{1w} and T_{2w} are the tuning voltages applied to the mass m_1 and mass m_2 along the W-axis; γ is an angle of the off-diagonal tuning electrodes.

The tuning procedure described in this section was performed at 0.1 mTorr pressure. Simulated frequency response curves for different voltages of the off-diagonal and diagonal tuning are shown in Figs. 11(a) and 12 (a), correspondingly. For the sensor excitation, 10 V DC voltage and 60 mV AC voltage were applied to the drive electrodes X1D of the inner mass. The DC voltages were applied to the electrodes (TY2A, TY2W) and (TY1A, TY1W) to modify the off-diagonal terms of the stiffness matrix, Fig. 11(b). To compensate for coupling between the modes, the DC voltage of 31 V was applied between the electrodes (TY2A, TY2W), while the DC voltage of 24.7 V was applied between the electrodes (Y1A, TY1W). This result is in good agreement with the analytically predicted values, Fig. 11(a).

In addition, the DC voltage of 50.7 V was applied to the electrodes Y2D to modify the diagonal terms of the stiffness matrix, enabling mode matching, Fig. 12(b). The predicted value of the DC voltage to be applied to these pair of electrodes was 46.1 V, which is in good agreement with the experiment, Fig. 12(a).

The coupling terms of the stiffness matrix, arising from the mechanical coupling of the two masses, are compensated during the simultaneous off-diagonal tuning and diagonal tuning.

During the following steps of higher precision tuning, when the resonant peaks of the gyroscope were tracked in the narrow range of frequencies, operational modes were tuned down to 50 mHz using the following DC voltages: TY2A–TY2W = 29.6 V; TY1A–TY1W = 24.7 V; Y2D = 50.7 V, Fig. 13.

In summary, the tuning procedure involves the following steps:

1. First, the modes mismatch and cross-coupling between modes are identified by fitting the experimental frequency response curves to the analytical solutions of the dual-mass system in presence of imperfections.
2. In the case when the aniso-elasticity angles α and $\beta > 22.5°$, the sensor re-wirebonding is necessary to switch the directions of the drive and tuning electrodes. Such angle means that the principal axes of elasticity are closer to the diagonal electrodes.
3. Tuning DC voltages for modification of the off-diagonal terms in the stiffness matrix are estimated analytically and the initial off-diagonal tuning is performed to remove the second (coupled mode) peak of the amplitude response curve.
4. Tuning DC voltages for modification of the diagonal terms in the stiffness matrix are estimated analytically and the initial coarse diagonal tuning is performed to reduce the frequency split between the operational modes to <3 Hz.
5. Tuning DC voltages for modification of the off-diagonal terms in the stiffness matrix are estimated again and the off-diagonal tuning is performed to remove the second (coupled mode) peak of the amplitude response curve.

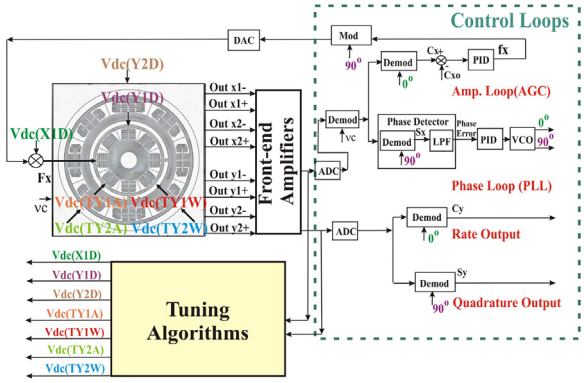

Fig. 14. System-level schematic of control electronics for gyroscope open-loop operation.

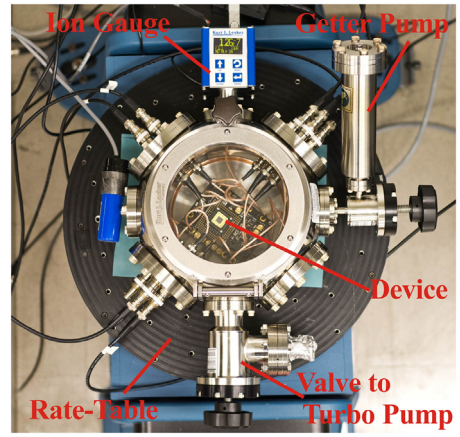

Fig. 15. The angular rate response was obtained in vacuum at 0.1 μTorr pressure.

6. Tuning DC voltages for modification of the diagonal terms in the stiffness matrix are estimated analytically and the fine diagonal tuning is performed to reduce the frequency split between the operational modes until the ratio between the second (coupled mode) peak and the first (drive mode) peak of the amplitude response curve becomes >0.1 or the modes are matched.
7. Steps 5 and 6 are repeated until the minimal frequency split between the modes is achieved. To achieve high precision, for the sensor presented in this manuscript, identification of the necessary tuning voltages has been performed three times for the off-diagonal tuning and three times for the diagonal tuning.

5. Gyroscope angular rate response and noise characterization

In order to evaluate the sensor performance before and after the electrostatic tuning, the dynamic response of the gyroscopes was obtained. To derive the sensor scale factor, the Ideal Aerosmith 2102 Series Two-Axis Position and Rate Table System was used to produce a reference rotation with programmed sinusoidal angular acceleration. The gyroscope was excited with a constant DC voltage and an AC voltage generated by a Phase Locked Loop (PLL), Fig. 14. A carrier signal ν_c at frequency of 100 kHz was applied to the proof-mass, resulting in the amplitude modulation of the sensor output. The output signal was then demodulated to reveal the low frequency changes in capacitance. The amplitude of the drive-mode motion was stabilized using an Automatic Gain Control (AGC) [41]. All loops were realized using a Zurich Instruments HF2LI digital lock-in amplifier.

The tuning procedure, described in Section 4, was repeated in a low out-gassing vacuum chamber at 0.1 μTorr pressure level, Fig. 15. Gyroscope characterization was performed in an open loop configuration. The response to the sinusoidal input of the rate table with frequency 1 Hz and 10° amplitude is shown in Fig. 16. The rate table characterization of the sensor before and after the electrostatic tuning of the operational modes, showed an increase in the scale factor by more than an order of magnitude, from 0.275 mV/deg/s to 4.82 mV/deg/s.

The Root Allan Variance Analysis (r-AVAR) was used to experimentally identify the random noise characteristics of the sensor. Noise analysis of the gyroscope, before and after tuning, showed the reduction in in-run bias stability, from 25.3°/h to 1.72°/h and the reduction in ARW, from 1.18°/$\sqrt{h}$ to 0.16°/$\sqrt{h}$, Fig. 17.

Experimental testing of the gyroscope, revealed an increased scale factor, reduced quadrature error, and improved noise characteristics after electrostatic compensation for structural imperfections, Table 2.

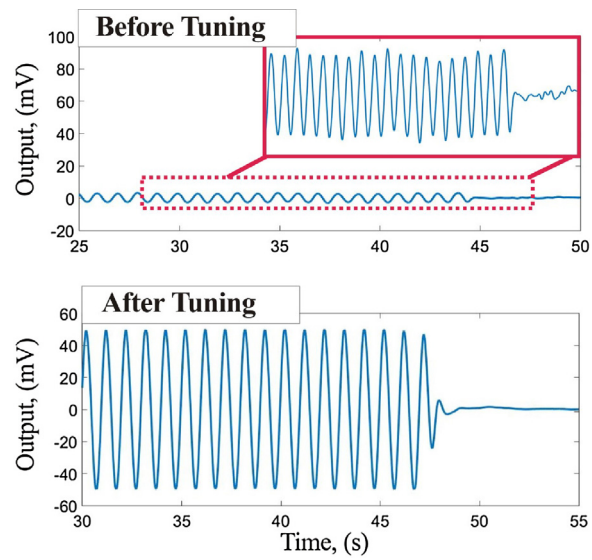

Fig. 16. Gyroscope response to sinusoidal input of the rate table, showing 17.5× higher SF and a stable amplitude after tuning.

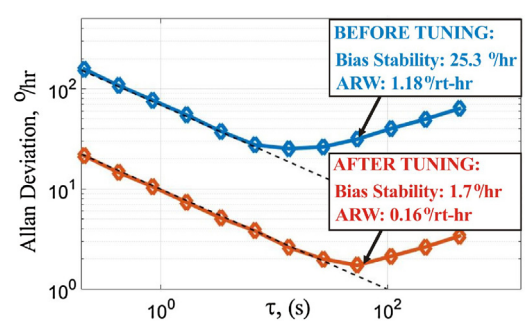

Fig. 17. Noise analysis of the gyroscope before and after tuning revealed reduction in bias stability, from 25.3°/h to 1.7°/h and reduction in ARW, from 1.18°/$\sqrt{h}$ to 0.16°/$\sqrt{h}$.

Table 2
Experimentally tested parameters of design I gyroscope.

Parameter	Before tuning	After tuning
Frequency split (Δf), Hz	26	<0.05
Quadrature error, dps	521	2.59
Scale factor, mV/dps	0.275	4.82
ARW, °/$\sqrt{h}$	1.18	0.16
Bias stability, °/h	25.3	1.72

The sensor presented in this paper is a first demonstration of a dynamically amplified gyroscope. Optimization of a nominal gap, sense capacitance, design- and material-limited quality factor are required for lower noise. For improved performance, the tuning algorithm described in this paper, can be applied to the sensors with an optimized design of the structural element and a lower level of as-fabricated imperfections.

6. Conclusion

Different designs of multi-mass gyroscopes have been extensively studied in literature. Multi-mass dynamically coupled systems offer advantages, such as dynamic balance, increased bandwidth, and dynamic amplification. However, the increased number of DOF of a mechanical element results in a more complex form of the structural stiffness matrix, as compared to a conventional single-mass gyroscope. Hence, more complex techniques have to be considered for electrostatic frequency tuning of operational modes in the case of a non-ideal multi-mass structural element.

In this work, a DC tuning technique, similar to a method commonly used for tuning a conventional single-mass gyroscope, has been employed for precision mode-matching of an imperfect dual-mass sensor. The analytical model of a dual-mass system in presence of imperfections has been explored and a method of electrostatic frequency trimming in a dual-mass gyroscope has been proposed. The tuning procedure is based on estimation of the modes mismatch and coupling between the modes, utilizing the experimental frequency response data. The analytical model is then used to determine the necessary tuning voltages to permit the removal of anisoelasticity and the mismatch of principal axes of stiffness, thus enabling the gyroscope operational modes to be matched.

Results of simulation were verified using experimental electrostatic frequency tuning of a dynamically amplified gyroscope. The coupling between the drive and sense modes was compensated and the frequency split between the modes was reduced from 26 Hz down to 50 mHz, resulting in 17.5× increase in the scale factor of the gyroscope.

The presented electrostatic compensation method can be used for off-line tuning of the gyroscope in the laboratory environment. Once a device is packaged and mounted within the measurement platform, the identified values of tuning DC voltages can be used as a starting point for on-line tuning. However, the packaging stresses often introduce additional frequency splitting and coupling between the operational modes of the sensor. In this case, the described compensation procedure has to be repeated in real time for on-line calibration.

It is important to notice that the analytical model presented in Section 4 accounts for imperfections in gyroscope's suspension, but does not take into consideration the imperfections of the proof masses and damping mismatches between the operational modes. The simplified model was shown to be sufficient for tuning the modes down to 50 mHz. However, an extended dynamical model might be necessary for the ultra-high precision tuning.

Similar to a single-mass device, in a dual-mass dynamically amplified gyroscope, external vibrations can induce undesirable displacements of the proof-masses effecting the mode-tuning parameters and creating significant bias and scale factor errors. The gyroscope designs utilizing multiple proof-masses vibrating in anti-phase and enabling common mode rejection of accelerations might be used to compensate for vibration sensitivity. Such idea was implemented, for example, in Tuning Fork Gyroscope [2], Quadruple Mass Gyroscope [3], and Dual Foucault Pendulum [1]. Future research directions include the design and development of a dynamically amplified gyroscope with multiple proof-masses for improved vibration immunity. In this manuscript, however, we limited our scope to introduction of an initial prototype of the dual-mass device and demonstration of the tuning method.

Acknowledgements

This material is based on work supported by the Defense Advanced Research Projects Agency and U.S. Navy under Contract No. N66001-16-1-4021. Devices were designed and tested in UCI MicroSystems Lab.

References

[1] D. Senkal, A. Efimovskaya, A.M. Shkel, Dual Foucault Pendulum gyroscope, in: IEEE International Conf. on Solid-State Sensors, Actuators and Microsystems (Transducers'2015), Alaska, USA, June 21–25, 2015.
[2] J. Bernstein, S. Cho, A.T. King, A. Kourepenis, P. Maciel, M. Weinberg, A micromachined comb-drive tuning fork rate gyroscope, in: Proc. IEEE International Conf. on Micro Electro Mechanical Systems (MEMS'1993), Fort Lauderdale, FL, USA, USA, February 10–10, 1993.
[3] A. Trusov, A. Schofield, A.M. Shkel, Micromachined rate gyroscope architecture with ultra-high quality factor and improved mode ordering, J. Sens. Actuators A: Phys. 165 (1) (2011) 26–34.
[4] C. Acar, A.M. Shkel, Inherently robust micromachined gyroscopes with 2-DOF sense-mode oscillator, IEEE J. Microelectromech. Syst. 15 (2) (2006) 380–387.
[5] C. Painter, A.M. Shkel, Dynamically Amplified Rate Integrating Gyroscopes, U.S. Patent 6,928,874, 2005.
[6] C. Painter, A.M. Shkel, Dynamically amplified rate integrating gyroscopes, in: Proc. NSTI Nanotechnology Conference and Trade Show Nanotech 2003, San Francisco, CA, USA, February 23–27, 2003.
[7] J.I. Seeger, B.E. Boser, Parallel-plate driven oscillations and resonant pull-in, in: Proc. Solid-State Sensor, Actuator and Microsystems Workshop, Hilton Head Island, South Carolina, June 2–6, 2002.
[8] A. Efimovskaya, Y. Lin, D. Wang, A.M. Shkel, Electrostatic compensation of structural imperfections in dynamically amplified dual-mass gyroscope, in: Proc. IEEE Inertial Sensors 2017, Kauai, HI, USA, March 27–30, 2017.
[9] B. Gallacher, J. Hedley, J.S. Burdess, A.J. Harris, M.E. McNie, Multi-modal tuning of a vibrating ring using laser ablation, Mech. Eng. Sci. J. Inst. Mech. Eng. 217 (2003) 1503–1513.
[10] K. Zhao, L. Feng, Q. Wang, M. Liu, B. Wang, F. Cui, Y. Sun, Suppressing the mechanical quadrature error of a quartz double-H gyroscope through laser trimming, IOP Chin. Phys. J. 22 (11) (2013).
[11] T. Lam, R. Darling, Modeling of focused ion beam trimming of cantilever beams, in: Proc. 3rd Int. Conf. Modelling and Simulation of Microsystems, San Diego, CA, USA, March 27–29, 2000.
[12] D. Joachim, L. Lin, Selective polysilicon deposition for frequency tuning of MEMS resonators, in: Proc. IEEE International Conf. on Micro Electro Mechanical Systems (MEMS'2002), Las Vegas, NV, USA, 24–24 January 2002, 2002, pp. 727–730.
[13] D.M. Schwartz, D. Kim, P. Stupar, J. DeNatale, R.T. MCloskey, Modal parameter tuning of an axisymmetric resonator via mass perturbation, IEEE J. Microelectromech. Syst. 24 (3) (2015) 545–555.
[14] T. Remtema, L. Lin, Active frequency tuning for microresonators by localized thermal stressing effects, in: Solid-State Sensor Actuator Workshop, Hilton Head Island, SC, –June 4–8, 2000, pp. 363–366.
[15] E. Tatar, S. Alper, T. Akin, Quadrature-error compensation and corresponding effects on the performance of fully decoupled MEMS gyroscopes, IEEE J. Microelectromech. Syst. 21 (3) (2012) 656–667.
[16] Z. Hu, B. Gallacher, J. Burdess, C. Fell, K. Townsend, Precision mode matching of MEMS gyroscope by feedback control, in: Proc. IEEE Sensors'2011 Conf, Limerick, Ireland, October 28–31, 2011.
[17] J. Jeltema, G. Cevat, Adaptive resonance tuning through feedback, in: American Control Conf, Portland, OR, USA, –June 8–10, 2005.
[18] C. Painter, A.M. Shkel, Active structural error suppression in MEMS vibratory rate integrating gyroscopes, IEEE Sens. J. 3 (5) (2003) 595–606.
[19] Z.X. Hu, B.J. Gallacher, J.S. Burdess, S.R. Bowles, H.T.D. Grigg, A systematic approach for precision electrostatic mode tuning of a MEMS gyroscope, IOP J. Micromech. Microeng. 24 (12) (2014).
[20] B.J. Gallacher, J. Hedley, J.S. Burdess, A.J. Harris, A. Rickard, D.O. King, Electrostatic correction of structural imperfections present in a microring gyroscope, IEEE J. Microelectromech. Syst. 14 (2) (2005) 221–234.
[21] J. Zhang, Y. Su, Q. Shi, A.-P. Qiu, Microelectromechanical resonant accelerometer designed with a high sensitivity, IEEE Sens. J. 15 (2015) 30293–30310.
[22] I. Zeimpekis, I. Sari, M. Kraft, Characterization of a mechanical motion amplifier applied to a MEMS accelerometer, J. Microelectromech. Syst. 21 (5) (2012) 1032–1042.
[23] T. Juneau, A. Pisano, J. Smith, Dual axis operation of a micromachined rate gyroscope, in: Proc. Int. Solid-State Sensors, Actuators and Microsystems Conf. (Transducers'97), Chicago, IL, USA, – June 19-19, 1997.

[24] S. Adamsy, F. Bertsch, K. Shaw, P. Hartwell, F. Moon, N. MacDonald, Capacitance based tunable resonators, J. Micromech. Microeng. 8 (1998) 15–23.
[25] F. Ayazi, K. Najafi, A HARPSS polysilicon vibrating ring gyroscope, IEEE J. Microelectromech. Syst. 10 (2) (2001) 169–179.
[26] N. Chekurov, L. Aaltonen, J. Gronicz, M. Kosunen, I. Tittonen, Design and fabrication of a tuning fork shaped voltage controlled resonator with additional tuning electrodes for low-voltage applications, in: Proc. Eurosensors XXIV, Linz, Austria, September 5–8, 2010.
[27] I. Prikhodko, A. Trusov, A.M. Shkel, Compensation of drifts in high-Q MEMS gyroscopes using temperature self-sensing, J. Sens. Actuators A: Phys. 201 (October) (2013) 517–524.
[28] D. Senkal, S. Askari, M.J. Ahamed, E. Ng, V. Hong, Y. Yang, C. Hyuck Ahn, T.W. Kenny, A.M. Shkel, 100k Q-factor toroidal ring gyroscope implemented in wafer-level epitaxial silicon encapsulation process, in: Proc. IEEE International Conf. on Micro Electro Mechanical Systems (MEMS'2014), San Francisco, CA, USA, January 26–30, 2014.
[29] J. Cho, J. Gregory, K. Najafi, High-Q, 3 kHz single-crystal silicon cylindrical rate-integrating gyro (CING), in: Proc. IEEE International Conf. on Micro Electro Mechanical Systems (MEMS'2012), Paris, France, 29 January–2 February, 2012, pp. 172–175.
[30] J. Cho, J. Woo, J. Yan, R. Peterson, K. Najafi, Fused-silica micro birdbath resonator gyroscope (μ-BRG), IEEE J. Microelectromech. Syst. 23 (1) (2014) 66–77.
[31] P. Shao, C.L. Mayberry, X. Gao, V. Tavassoli, F. Ayazi, A polysilicon microhemispherical resonating gyroscope, IEEE J. Microelectromech. Syst. 23 (4) (2014) 762–764.
[32] P. Taheri-Tehrani, T.-H. Su, A. Heidari, G. Jaramillo, C. Yang, S. Akhbari, H. Najar, S. Nitzan, D. Saito, L. Lin, D.A. Horsley, Micro-scale diamond hemispherical resonator gyroscope, in: Proc. IEEE Solid-State Sens., Actuators, Microsyst. Workshop, Hilton Head Island, SC, USA, June, 2014, pp. 289–292.
[33] D. Senkal, M.J. Ahamed, A.A. Trusov, A.M. Shkel, Achieving sub-Hz frequency symmetry in micro-glassblown wineglass resonators, IEEE J. Microelectromech. Syst. 23 (February (1)) (2014) 30–38.
[34] C. Painter, A. Shkel, Identification of anisoelasticity for electrostatic trimming of rate integrating gyroscopes, in: Proc. 2002 SPIE Annual International Symposium on Smart Structures and Materials, San Diego, CA, March 17, 2002.
[35] A.S. Phani, A.A. Seshia, Identification of anisoelasticity and nonproportional damping in MEMS gyroscopes, in: Proc. NSTI Nanotechnology Conference and Trade Show Nanotech 2004, Boston, Massachusetts, USA, March 7–11, 2004.
[36] D.D. Lynch, Coriolis vibratory gyros, in: Proc. Symposium Gyro Technology, Stuttgart, Germany, 1998, pp. 1.0–1.14.
[37] D. Wang, M. Asadian, A. Efimovskaya, A.M. Shkel, A comparative study of conventional single-mass and amplitude amplified dual-mass MEMS vibratory gyroscopes, in: Proc. IEEE Inertial Sensors 2017, Kauai, HI, USA, March 27–30, 2017.
[38] V. Kaajakari, Practical MEMS, Small Gear Publishing, Las Vegas, NV, 2009.
[39] D.D. Lynch, Vibratory gyro analysis by the method of averaging, in: Proc. 2nd St. Petersburg Conf. on Gyroscopic Technology and Navigation, St. Petersburg, Russia, 1995, pp. 26–34.
[40] J. Giner, Y. Zhang, D. Maeda, K. Ono, A.M. Shkel, T. Sekiguchi, Dynamically balanced degenerate mode gyro with sub-Hz frequency symmetry and temperature robustness, in: Proc. IEEE International Conf. on Micro Electro Mechanical Systems (MEMS'2017), Las Vegas, NV, USA, January 22–26, 2017, pp. 1103–1106.
[41] I. Prikhodko, S. Zotov, A. Trusov, A.M. Shkel, What is MEMS gyrocompassing? Comparative analysis of maytagging and carouseling, IEEE/ASME J. Microelectromech. Syst. 22 (6) (2013) 1257–1266.

Biographies

Alexandra Efimovskaya is currently a graduate student researcher at the Micro Systems Laboratory, University of California Irvine, working towards a Ph.D. in mechanical engineering with a focus on micro-electro-mechanical (MEMS) inertial sensors and systems. The main area of her research is related to design and control of inertial sensors for navigation applications. She received a Diploma (Hons.) degree in engineering specializing in navigation systems from the Saint-Petersburg State University of Aerospace Instrumentation, Saint-Petersburg, Russia, in 2009, and a M.S. degree in mechanical and aerospace engineering from the University of California, Irvine, CA, USA, in 2015. She was a 2011 Fulbright Scholar and the recipient of the 2015Amelia Earhart Award for women in aerospace-related science. She won the Outstanding Paper Award (oral presentation category) at the 18th International Conference on Solid-State Sensors, Actuators and Microsystems (Transducers'2015), and the Best Student Paper Award (lecture track) at the IEEE/ASME International Symposium on Inertial Sensors (Inertial'2017).

Danmeng Wang received the B.S. degree in Electrical Engineering from Beijing Jiaotong University, Beijing, China, in 2013, and the M.S. degree in Electrical Engineering and Computer Science from University of California Irvine, CA, USA, in 2017. She is currently pursuing the Ph.D. degree in Electrical Engineering and Computer Science in University of California Irvine. Her research interests include design and fabrication of MEMS inertial sensors.

Yu-Wei Lin received the B.S. degree in engineering mechanics from University of Illinois at Urbana Champaign, IL, USA, in 2014, and the M.S. degree in mechanical engineering from University of California Irvine, CA, USA, in 2016. He is currently pursuing the Ph.D. degree in mechanical engineering in University of California Irvine. His research interests include design, fabrication, and control of vibratory inertial sensors.

Andrei M. Shkel (F'99) received the Diploma (Hons.) degree in mechanics and mathematics from Moscow State University, Moscow, Russia, in 1991, and the Ph.D. degree in mechanical engineering from the University of Wisconsin, Madison, WI, USA, in 1997. In 2000, he joined the Faculty of the University of California at Irvine, Irvine, CA, USA, where he is currently a Professor with the Department of Mechanical and Aerospace Engineering, with a joint appointment with the Department of Electrical Engineering and Computer Science, and the Department of Biomedical Engineering. He served as a Program Manager of the Microsystems Technology Office at the Defense Advanced Research Projects Agency (DARPA), Arlington, VA, USA, from 2009 to 2013. His professional interests, reflected in over 200 publications, include solid-state sensors and actuators, microelectromechanical systems-based neuroprosthetics, sensor-based intelligence, and control theory. He holds over 30 U.S. and worldwide patents. His current interests center on the design, manufacturing, and advanced control of high-precision micromachined gyroscopes. He was a recipient of the 2002 George E. Brown, Jr. Award, the 2005 NSF CAREER Award, the 2006 UCI HSSoE Best Faculty Research Award, and the 2009 IEEE Sensors Council Technical Achievement Award. He received the Office of the Secretary of Defense Medal for Exceptional Public Service for his work at DARPA as a Program Manager in 2013. He has served on a number of Editorial Boards, most recently, as an Editor of the IEEE/ASME JOURNAL OF MICROELECTROMECHANICAL SYSTEMS and the Founding Chair of the IEEE International Symposium on Inertial Sensors and Systems. Dr. Shkel is the IEEE Fellow and was voted 2018 president-elect of the IEEE Sensors Council.